Supporting Information for "Theoretical Stability of Ice Shelf Basal Crevasses with a Vertical Temperature Profile"

N. B. Coffey[1,2], C. Y. Lai[1,2,3], Y. Wang[3], W. R. Buck[4], T. Surawy-Stepney[5], A. E. Hogg[5]

[1]Department of Geophysics, Stanford University, Stanford, CA, USA

[2]Program in Atmospheric and Oceanic Sciences, Princeton University, Princeton, NJ, USA

[3]Department of Geosciences, Princeton University, Princeton, NJ, USA

[4]Lamont-Doherty Earth Observatory of Columbia University, New York, NY, USA

[5]School of Earth and Environment, University of Leeds, Leeds, UK

Contents of this file

1. Text S1: Methods.
2. Text S2: Temporal Observation of a Basal Crevasse to Rift Transition.
3. Text S3: Nye's Zero-Stress for Rift Formation via Basal Crevasses.
4. Text S4: Derivation of Nye's with Horizontal Force Balance.
5. Text S5: Result Robustness: Robin Temperature Profile and Uncertainty Estimation.

---

6. Figure S1 shows the 1-dimensional (1D) regions of ice shelf flow on Ross and Larsen C ice shelves.

7. Figure S2 shows the effect of padding mélange ice thickness with locally-averaged unbroken ice thickness.

8. Figure S3 is the same as Figure 3 in the main text, except on Larsen C.

9. Figures S4 and S10 contain the estimates of stress in the extensional, approximately 1D regions that do not contain rifts assuming linear and Robin temperature profiles, respectively.

10. Figure S5 visualizes Nye's Zero-Yield Stress theory.

11. Figure S6 shows examples of the linear and Robin temperature profiles used in this study.

12. Figures S7 and S8 are the same as Figures 3 and S3, except that they use a Robin temperature profile instead of a linear temperature profile.

13. Figure S9 is the same idea as Figure 4, except that approximate rift stress estimates are included and both linear and Robin temperature profiles are shown.

14. Figure S11 contains upper bound estimates of measurement uncertainty on Ross and Larsen C ice shelves from remote-sensed data products.

S1 Methods

To create rift prediction maps, several important steps must be made to ensure sensible and causal predictions. First, we must validate that the areas containing rifts are in regions that largely obey the 1-dimensional (1D) extensional background flow assumptions of the fracture theories assessed in this study. To do so, we use automatic differentiation to construct strain rate fields based on MEaSUREs ice shelf velocity data (Rignot et al., 2011; Mouginot et al., 2012, 2017; Rignot et al., 2017).

To determine if the 1D fracture theory assumptions are upheld, we utilize the criterion that the normalized resistive stress difference between that of the SSA solution and that assuming 1D flow is within 10%,

$$\left|\frac{\overline{R}_{xx}^{SSA} - \overline{R}_{xx}^{1D}}{\overline{R}_{xx}^{1D}}\right| \leq 0.1, \tag{S1}$$

where $\overline{R}_{xx}^{SSA} = \overline{B}\dot{\epsilon}_e^{-1+\frac{1}{n}}\left(2\dot{\epsilon}_{xx} + \dot{\epsilon}_{yy}\right)$ and $\overline{R}_{xx}^{1D} = 2\overline{B}\dot{\epsilon}_{xx}^{\frac{1}{n}}$. This equation can be simplified and written in terms of dimensionless measures of strain rate,

$$\left|\left(1+\alpha^2+\alpha+\xi^2\right)^{\frac{1}{2n}-\frac{1}{2}}\left(1+\frac{\alpha}{2}\right)-1\right| \leq 0.1, \tag{S2}$$

where the first term with $\alpha = \frac{\dot{\epsilon}_{yy}}{\dot{\epsilon}_{xx}}$ and $\xi = \frac{\dot{\epsilon}_{xy}}{\dot{\epsilon}_{xx}}$ comes from the second invariant of the strain rate tensor under the 3D incompressible condition and assumption of negligible vertical shear stresses. Thus, while one could calculate the depth-averaged ice hardness $\bar{B}\left(T\right)$ assuming some vertical temperature profile, this is unnecessary as this term cancels and does not appear in equation (S2). Figure S1 shows the region which satisfy the criterion (S2), from which we may select our rifts.

Second, the rifts identified by (Walker et al., 2013) in these regions must have their thickness values padded to an estimate of the unbroken state thickness. These rifts are currently filled with a conglomerate ice material composed of sea ice, snow, and ice shelf fragments, collectively referred to as ice mélange (Rignot & MacAyeal, 1998; MacAyeal et al., 1998; Hulbe et al., 1998). Since our goal is to predict if the observed rift could have formed, rather than the stability of the mélange in the rift, we need to estimate the state of the unbroken ice. Here, we generate bounding boxes around rifts of interest and infill the mélange thickness with an average of the local unbroken ice thickness in BedMachine Version 2 (Morlighem, 2020; Morlighem et al., 2020), as shown in Figure S2. Combined with the map of regions that uphold the 1D extensional flow assumption of our fracture theories in Figure S1, we generate rift prediction maps in Figures 3 and S3.

The caveat to this method is that in the absence of remotely sensed data on the time-dependent evolution of basal crevasses into rifts, strain rates and temperature profiles at the time of the basal crack to rift transition remain unknown. We present an analysis of time series data in Text S2, but this data is largely unavailable for many existing rifts. As such, we utilize the modern values of surface temperatures and strain rates from (van Wessem et al., 2018) and (Wearing, 2017), acknowledging that these may have changed since rift formation. We note that the $1/n$ exponent dependence of strain rate given Glen's flow law in equation (3) shields the resistive stress from strain rate changes, thus decreasing the sensitivity to precise strain rate estimates.

Due to the uncertainty associated with the temperature and strain rate evolution since the time of rift formation, we construct data sets of stress estimates on the non-rift ice shelf regions, as shown in Figure S4. The advantage of these data sets is that they do not have the time-evolution problem of rift data sets. Therefore, given our methods, we have more confidence in a theory that correctly predicts many rifts and minimally overpredict rifts than a theory which correctly predicts most or all rifts while overpredicting rifts in non-rift regions. In our work, this emphasizes that LEFM with depth-averaged resistive stress (Zarrinderakht et al., 2022) has too low of a threshold for rift initiation.

We note that since (Walker et al., 2013) do not necessarily identify all rifts in their rift catalog, there could be rifts included in our non-rift region data sets. To help remove rifts not classified by (Walker et al., 2013) in the non-rift regions of Figure S4, we exclude data that would unanimously be predicted a rift in every fracture theory presented in this study. As such, we take the highest stress threshold for rifting in Nye's Zero-Stress theory with isothermal depth-averaged resistive stress, $\overline{R}^{*}_{xx}/\overline{R}^{IT}_{xx} = 2$. This is reflected in the magnitude of the color bar of Figure S4.

S2 Temporal Observation of a Basal Crevasse to Rift Transition

Figures 1 c) and e) show the ratio of depth-averaged resistive stress to isothermal ice tongue resistive stress $\overline{R}_{xx}/R^{IT}_{xx}$ over Pine Island Ice Shelf in January and May 2019 respectively. The resistive stress was found using eq. (7) with along-flow strain rates estimated from 200 $\times$ 200 m resolution, monthly-averaged ice velocity observations made using feature tracking applied to Sentinel-1 image pairs (Wuite et al., 2021) (https://cryoportal.enveo.at/data/). The strain rate components were calculated via numerical differentiation of the easting and northing velocities using methods developed in Chartrand (2017). Estimates of ice shelf thickness were according to BedMachine version 2 (Morlighem, 2020), and the temperature profile was assumed to be linear between -2°C at the ice shelf base and temperature given by RACMO (van Wessem et al., 2018) at the surface. The accompanying satellite images shown in d) and f) are geocoded, multi-looked and radiometrically terrain-corrected Single-Look Complex backscatter data from the European Space Agency and European Commission Copernicus' Sentinel-1 satellites - shown at 50 m resolution.

These show the concurrent evolution of the ratio of stresses near the terminus of the ice shelf alongside the evolution of a rift, likely from a central basal crevasse (Jeong et al., 2016), that eventually led to the calving of the B49 iceberg in February 2020. We see clear changes to the along-flow strain rates over the rift as it widens and propagates laterally. This provides a motivating example for determining stress conditions under which basal crevasses transition into rifts, such as those discussed in this article. However, Figures 1 c) and e) show that we measure stress ratios below those required for full-thickness rifts according to each of the theories discussed in this article. I.e. the stress ratio over the rift that is clearly visible by May 2019 (fig. 1 f) is below the value of 1 predicted by Nye's Zero-Yield Stress criterion, modified to maintain horizontal force balance (eq. (16)). However, Figure 1 should not be seen as an example aimed at validation of one of the theories considered here, merely as motivation for the work. In part, this is because the central part of Pine Island Ice Shelf does not conform to the assumption of one-dimensional flow (eq. (S2)) (though the speed of the ice tongue varies little laterally, the flow is dominated by advection and across-flow strain rates are similar in magnitude to along-flow strain rates), nor is the ice shelf cavity necessarily hydrostatic with temperature $T = -2°\mathrm{C}$. Additionally, by using satellite-derived measures of ice velocity averaged over monthly intervals, we cannot hope to capture the maximum strain rates over a crevasse of this scale as the data is too limited in both spatial and temporal resolution. In the future, a validation of the theories discussed in this article using time series of strain rate or stress data should be carried out with the use of higher-resolution satellite data or data collected on the ground, e.g. with the use of an ApRES system (Nicholls et al., 2015). Similarly, it is not possible to accurately determine when the crevasse transitioned into a rift from satellite images alone, or whether it was ever a basal crevasse at all. Future work that aims to use time series data should do so in conjunction with other datasets that provide further information on the type of crevasse under consideration.

S3 Nye's Zero-Stress for Rift Formation via Basal Crevasses

Nye's Zero-Yield Stress (Nye, 1955) argues that a vertical crack will propagate so long as there is no net compression of the net longitudinal stress σ_n at the crack tip. Written mathematically, the Zero-Yield Stress condition ($\sigma_c = 0$) claims that a crack propagates when

$$\sigma_n \geq \sigma_c. \tag{S3}$$

Under Nye's theory, a basal crevasse will form a rift when the criterion (S3) holds for all depths. The criterion can also be re-written in terms of a dimensionless resistive stress, with $z = 0$ at the bottom of the ice,

$$\frac{R_{xx}}{\left(\rho_w - \rho_i\right) gH} \geq \begin{cases} \frac{z}{H} & 0 \leq \frac{z}{H} \leq \frac{\rho_i}{\rho_w} \quad \text{(below sea level)} \\ \frac{\rho_i}{\rho_w - \rho_i}\left(1 - \frac{z}{H}\right) & \frac{\rho_i}{\rho_w} \leq \frac{z}{H} \leq 1 \quad \text{(above sea level)} \end{cases} \tag{S4}$$

as visualized by the red dotted lines in Figure S5, which allows us to determine basal crevasse depth and rift formation.

Since Nye's original theory has zero material strength, the minimum required resistive stress to form a rift is defined by equation (S4). If the resistive stress is not in net tension at the ice shelf base, no basal crevasse is predicted. If the resistive stress is in net tension at the base but becomes less than the dotted red curve in Figure S5 at a larger height $z > 0$, the point of equality below sea level is the basal crevasse depth. For example, if the resistive stress takes the value shown by the dashed green line of Figure S5, a basal crevasse would propagate up to a depth about 60% of the unbroken ice thickness. However, resistive stresses that are greater than or equal to the dotted red curve for all heights will form rifts because basal crevasses can propagate all the way to the surface. Figure S5 clearly demonstrates the underestimation of rifts when depth-averaged resistive stress theories, the dashed lines, are used instead of their depth-dependent counterparts, the solid curves.

Next, we develop the mathematical expression for the rift initiation stress threshold of Nye's theory. These expressions are plotted in dashed blue and solid green in Figures 4 and S9. Taking the assumption that the second invariant of strain rate is approximately the along-flow strain rate for consistency with LEFM, the rift formation criteria given isothermal, depth-averaged resistive stress can be written as a dimensionless stress ratio,

$$\frac{\overline{R}_{xx}}{\overline{R}_{xx}^{IT}} \geq 2, \tag{S5}$$

with $\overline{R}_{xx}^{IT} = \frac{1}{2}\left(1 - \frac{\rho_i}{\rho_w}\right)\rho_i g H$ the depth-averaged ice tongue resistive stress. This equation can be understood visually from Figure S5 as the corner of the dotted red curve located on the x-axis at $\frac{R_{xx}}{(\rho_w - \rho_i) g H} = \frac{\rho_i}{\rho_w} \approx 0.89$, which is equivalent to (S5). Similarly, in the depth-dependent case, we have that

$$\frac{\overline{R}_{xx}}{\overline{R}_{xx}^{IT}} \geq 2\frac{\rho_w}{\rho_i}\frac{d_b^*}{H}\frac{\overline{\tilde{B}}(T)}{\tilde{B}(T(\frac{d_b^*}{H}))}. \tag{S6}$$

Here $\tilde{B}\left(T\right) = B\left(T\right)/B\left(T = -2°\mathrm{C}\right)$ is the dimensionless ice hardness, $\overline{\tilde{B}}\left(T\right)$ is the depth-averaged dimensionless ice hardness, and d_b^* is the unstable basal crevasse depth at which a basal crevasse will propagate to form a rift. The unstable basal crevasse depth d_b^* depends upon temperature gradient and the prescribed stresses. For isothermal ice, the unstable basal crevasse height is sea level without tides, $d_b^* = \frac{\rho_i}{\rho_w}H$, and we also have

$\overline{\tilde{B}}(T) = \tilde{B}(T(\frac{d_b^*}{H}))$ so the above equation (S6) reduces to the depth-averaged case in equation (S5). For vertical temperature profiles that become colder towards the ice shelf surface, the unstable basal crevasse depth d_b^* can decrease. Given the ice hardness function of (LeB. Hooke, 1981) and a linear temperature profile from $T_b = -2°\text{C}$ at the base, the unstable basal crevasse depth d_b^* falls below sea level for surface temperatures at least as cold as $T_s = -25°\text{C}$ in Nye's original theory as well as Nye's with HFB, as shown with the blue curves of Figure 2(a) with $T_s = -32°\text{C}$.

S4 Derivation of Nye's with Horizontal Force Balance

Here we demonstrate how Nye's theory does not uphold horizontal force balance on an isothermal ice shelf through an Eulerian control volume argument based on (Buck, 2023), also see Section 2.3. The main argument of the control volume approach, as has been applied by (Weertman, 1957) and (Jezek, 1984) to solve for the net tension we call $\overline{R}_{xx}^{IT}$ at ice fronts, is Newton's Second Law. The sum of the forces acting on the control volume are equal to the product of mass and acceleration of fluid entering the control volume. In our case, there is no net acceleration of fluid into or out of the control volume, and the shear stresses on surface and bottom boundaries are negligible. Thus, we can write the horizontal force balance for a control volume between a crevassed location $x = x_c$ and an uncrevassed downstream location $x = x_c + \Delta x$ as

$$\int_0^H \left[\sigma_{xx}\left(x_c + \Delta x, z\right) - \sigma_{xx}\left(x_c, z\right)\right] dz = 0. \tag{S7}$$

The horizontal force balance model for an isothermal ice shelf was developed in (Buck, 2023) and is summarized below. At the downstream location $x = x_c + \Delta x$ that is sufficiently far away from the bending stresses near the ice front (Reeh, 1968; Wagner et al., 2016), we have

$$\sigma_{xx}\left(x_c+\Delta x, z\right)=-\rho_i g\left(H-z\right)+R_{xx}\left(x_c+\Delta x\right). \tag{S8}$$

At the crevassed location, we will follow Nye's Zero-Yield Stress assumption and have dual surface and basal crevasses with depths d_s and d_b,

$$\sigma_{xx}\left(x_c, z\right)=\left\{\begin{array}{lr} 0, & H-d_s \leq z \leq H \\ -\rho_i g\left(H-z\right)+R_{xx}\left(x_c\right) & d_b \leq z \leq H-d_s \\ -\rho_w g\left(z_h-z\right), & 0 \leq z \leq d_b \end{array}\right\}. \tag{S9}$$

Note that the stresses cannot be the same at both locations, or $\sigma_{xx}\left(x=x_c\right) \neq \sigma_{xx}\left(x=x_c+\Delta x\right)$, because the intact ice is effectively thinner at the crevassed location. If we were to evaluate the force balance of equation (S7) with the incorrect assumption of $\sigma_{xx}\left(x=x_c\right)=\sigma_{xx}\left(x=x_c+\Delta x\right)$, the crack depths would be twice as deep as that of Nye's original theory,

$$d_s=\frac{2R_{xx}}{\rho_i g}, d_b=\frac{2R_{xx}}{\left(\rho_w-\rho_i\right)g}, \tag{S10}$$

and the stress distribution at the surface crevasse tip would not be continuous, $\sigma_{xx}(z=H-d_s)=-\rho_i g d_s+R_{xx}\neq 0$. Thus, to satisfy a continuous stress at the surface crack tip, we have

$$R_{xx}\left(x=x_c\right)=\rho_i g d_s. \tag{S11}$$

Similarly, using stress continuity at the basal crack tip gives a relation between surface and basal crack depths,

$$\left(\rho_w-\rho_i\right)d_b=\rho_i d_s. \tag{S12}$$

With the crack depth relation in equation (S12), plugging the stress definitions in equations (S8), (S9), (S11) into the force balance condition of equation (S7) yields the analytical crack depth predictions of (Buck, 2023) for an isothermal ice shelf,

$$\frac{d_b}{H} = \frac{\rho_i}{\rho_w}\left(1 - \sqrt{1 - \frac{R_{xx}\left(x_c + \Delta x\right)}{\overline{R}_{xx}^{IT}}}\right), \frac{d_s}{H} = \left(1 - \frac{\rho_i}{\rho_w}\right)\left(1 - \sqrt{1 - \frac{R_{xx}\left(x_c + \Delta x\right)}{\overline{R}_{xx}^{IT}}}\right). \tag{S13}$$

For more insight into the role of temperature dependence, we now specify the form of equations (14) and (15) for a simplified, approximate ice hardness function and linear vertical temperature gradient. In equation (4), the second term in the brackets, $-C/\left(T_r - T\right)^k$, is two to three orders of magnitude smaller than the first term, T_0/T. Similarly, with temperature $T\left(\tilde{z}\right) = T_b\left[1 - \left(1 - T_s/T_b\right)\tilde{z}\right]$ in Kelvin, the gradient term $\left(1 - T_s/T_b\right)\tilde{z}$ is at least an order of magnitude smaller than unity, so we may Taylor expand the exponent to first order in $\left(1 - T_s/T_b\right)\tilde{z}$. We define the approximated ice hardness function B_a with these two simplifications,

$$B_a\left(T\left(\tilde{z}\right)\right) \approx B_0 \exp\left[\frac{T_0}{T_b + \left(T_s - T_b\right)\tilde{z}}\right] \approx B_0 \exp\left[\frac{T_0}{T_b}\right] \exp\left[\frac{\tilde{z}}{\tilde{z}_0}\right], \tag{S14}$$

with the dimensionless e-folding decay length scale $\tilde{z}_0 \equiv \left(\frac{T_0}{T_b}\left(1 - \frac{T_s}{T_b}\right)\right)^{-1}$. Therefore, the crevasse depth relation of equation (14) may be written as

$$\tilde{d}_b = \tilde{d}_s \frac{\rho_i}{\rho_w - \rho_i} \exp\left[\frac{-\left(1 - \tilde{d}_s - \tilde{d}_b\right)}{\tilde{z}_0}\right], \tag{S15}$$

and the horizontal force balance of equation (15) may be written as

$$\frac{\overline{R}_{xx}}{\overline{R}_{xx}^{IT}} = \frac{\rho_w}{\rho_w - \rho_i}\tilde{d}_s^2 + \frac{\rho_w}{\rho_i}\tilde{d}_b^2 + \frac{\tilde{d}_s}{\frac{1}{2}\left(1 - \frac{\rho_i}{\rho_w}\right)}\tilde{z}_0\left(1 - \exp\left[\frac{-\left(1 - \tilde{d}_s - \tilde{d}_b\right)}{\tilde{z}_0}\right]\right). \tag{S16}$$

Even with the simplified ice hardness, these equations (S15) and (S16) are not algebraically solvable due to the nature of the Arrhenius equation. Although the result including vertically-varying temperature requires numerical treatment, the rift initiation stress threshold produced using (LeB. Hooke, 1981)'s ice hardness function is within 0.1%

of the analytical isothermal solution $\frac{\overline{R}^*_{xx}}{\overline{R}^{IT}_{xx}} = 1$ for all surface temperatures used for both linear and Robin (Text S5) temperature profiles. Therefore, we can well-approximate the rift initiation stress threshold as that of a freely-floating ice shelf without buttressing, i.e.

$$\frac{\overline{R}^*_{xx}}{\overline{R}^{IT}_{xx}} = 1. \tag{S17}$$

S5 Result Robustness: Robin Temperature Profile and Uncertainty Estimation

To confirm the robustness of our results given our data sources, we run through the analyses of this paper assuming a Robin temperature profile (Robin, 1955). While this solution is strictly valid for an ice divide, the curvature of the profile may be more appropriate compared to borehole data in some cases than a linear temperature profile (Thomas & MacAyeal, 1982; Rist et al., 2002; Tyler et al., 2013; Craven et al., 2009; Sergienko et al., 2013). Further, the goal of this exercise is not to create highly realistic temperature profiles by modeling the computationally expensive temperature evolution and advection from ice divides to ice shelves, but is instead meant as a sensitivity test of the results to the assumed temperature profile. As with the example plotted in Figure S6, the Robin family of temperature profiles have the form

$$T\left(\tilde{z}\right) = T_s + \frac{q}{k}\sqrt{\frac{\pi\kappa H_d}{2\dot{a}}}\left[\operatorname{erf}\left(\sqrt{\frac{\dot{a}H_d}{2\kappa}}\right) - \operatorname{erf}\left(\tilde{z}\sqrt{\frac{\dot{a}H_d}{2\kappa}}\right)\right], \tag{S18}$$

with surface temperature T_s, thermal diffusivity $\kappa \equiv \frac{k}{\rho_i c_p} \approx 10^{-6}\mathrm{m}^2/\mathrm{s}$ defined by thermal conductivity to ice density and specific heat of ice, rescaled vertical coordinate $\tilde{z} = \frac{z}{H}$ with value 0 at the ice base and 1 at the surface, basal heat flux q, ice divide thickness $H_d \approx 1000$ m, and snowfall rate $\dot{a} \approx 0.1$ m/yr based on (Fowler & Ng, 2020). We note that the influence for setting the ice divide thickness H_d is to match the (Sandhäger et al., 2005) profile, used to study the Larsen B breakup, near sea level as demonstrated in

Figure S6. We choose for the temperature profiles to match near sea level, as this region is important in determining if basal crevasses propagate to form rifts. Considering the ice-ocean temperature at the bottom of ice shelf $T_b = -2°\text{C}$, we have

$$T_b = T_s + \frac{q}{k}\sqrt{\frac{\pi\kappa H_d}{2\dot{a}}}\text{erf}\left(\sqrt{\frac{\dot{a}H_d}{2\kappa}}\right), \tag{S19}$$

Substituting (S19) into (S18) gives a simple form of the Robin profile,

$$T\left(\tilde{z}\right) = T_s + \left(T_b - T_s\right)\left(1 - \frac{\text{erf}\left(\tilde{z}\sqrt{\frac{\dot{a}H_d}{2\kappa}}\right)}{\text{erf}\left(\sqrt{\frac{\dot{a}H_d}{2\kappa}}\right)}\right). \tag{S20}$$

The remainder of the analyses for each theory is the same as presented in the body of this paper, with the exception that we include approximate stress in rifts in Figure S9 for linear and Robin temperature profiles. Viewing Figures S7, S8, S9, and S10, we see that the results have the same form in the Robin temperature profile case as the linear temperature profile case. Not only do the rift formation stress curves with linear and Robin temperature profiles in Figure S9 have similar form, but the relative accuracy of each theory is comparable in Figures S7, S8 versus 3, S3. Additionally, while there is slight surface temperature dependence to Nye's with Horizontal Force Balance with a linear temperature profile in Figure S9, the solution with a Robin temperature profile has the stress threshold of a freely-floating ice tongue for all surface temperatures sampled, making the stress threshold the same as the depth-averaged formulation of (Buck, 2023). Due to the colder temperatures and subsequent larger stress, the non-rift ice shelf data in Figure S10 may suggest a rift formation stress at or slightly larger than predicted by Nye's with Horizontal Force Balance on Larsen C. Overall, the conclusions of the paper with a linear temperature profile are unchanged given our estimate of a Robin temperature profile.

A discussion of result robustness is incomplete without considering the uncertainty in data products. The largest data uncertainty comes from the measurements of ice thickness (Morlighem, 2020; Morlighem et al., 2020), where the uncertainties in our regions of interest are 100 meters for the majority of the RIS, or around a third of the ice thickness, and around 30 meters for the LCIS, or about a tenth of the ice thickness. Alone, one standard deviation of this uncertainty would shift the data points up or down by about a third for RIS data or about a tenth for LCIS data on Figures 4, S9. As such, we look at LCIS for result robustness. Importantly, if the ice shelf data of interest is governed by the 1D SSA momentum equation (MacAyeal, 1989),

$$\partial_x \left(H\overline{R}_{xx} \right) = \rho_i g H \left(1 - \frac{\rho_i}{\rho_w} \right) \frac{\partial H}{\partial x}, \tag{S21}$$

then the depth-averaged resistive stress scales linearly with H. To compute uncertainty accurately for dependent variables, we would have to use covariance (Taylor, 1982); however we cannot meaningfully compute the covariance for each pixel of ice shelf data, and so we estimate the upper bound on uncertainty σ_β with

$$\sigma_\beta \leq \sqrt{\sum_i \left(\frac{\partial \beta}{\partial x_i} \sigma_{x_i} \right)^2} = \beta \sqrt{\left(\frac{\sigma_H}{H} \right)^2 + \left(\frac{\sigma_{\dot\epsilon_{xx}}}{n\dot\epsilon_{xx}} \right)^2 + \left(\frac{\partial B(T^*)}{\partial T^*} \frac{\sigma_{T^*}}{B(T^*)} \right)^2}. \tag{S22}$$

Here, our variable of interest is the dimensionless resistive stress $\beta = \overline{R}_{xx}/\overline{R}_{xx}^{IT}$. The uncertainties in thickness, strain rate, and equivalent temperature are $\sigma_H, \sigma_{\dot\epsilon_{xx}}$, and σ_{T^*}, with equivalent temperature T^* defined as the temperature at which $\overline{B} = B\left(T^*\right)$ (Sergienko, 2014). We take the strain rate uncertainty associated with 20km from the ice front from Table C.1 of (Wearing, 2017) and apply this to the whole ice shelf. Given that we do not have defined uncertainties associated with equivalent temperature, we estimate $\sigma_{T^*} = 3$K from the uncertainty range associated with modeled and observed RACMO surface temperature data in Figure 3a of (van den Broeke, 2008). In this calculation, we assume the Robin temperature profile in our ice hardness and equivalent temperature calculations, as we do not expect profiles warmer than linear, but this choice is negligible in the final results.

We plot the upper bound of dimensionless resistive stress uncertainty σ_β in Figure S11. Given the distributions of these datasets have some large outliers that skew the mean, we report the estimated median uncertainties for RIS and LCIS are $\sigma_\beta = 0.27$ and $\sigma_\beta = 0.14$, respectively. The RIS median uncertainty is large as anticipated, and the LCIS median uncertainty is comparable to the difference between LEFM with $R_{xx}(z)$ and Nye's with Horizontal Force Balance given the temperatures on LCIS (see red and cyan curves on Figures 4, S9). Therefore, more precise measurements of ice thickness, strain rate, and temperature are needed to further observationally constrain the optimal theory for tensile rift initiation from basal crevasses.

References

Buck, W. R. (2023). The role of fresh water in driving ice shelf crevassing, rifting and calving. *Earth and Planetary Science Letters*, *624*, 118444. Retrieved from `https://www.sciencedirect.com/science/article/pii/S0012821X23004570` doi: https://doi.org/10.1016/j.epsl.2023.118444

Chartrand, R. (2017). Numerical differentiation of noisy, nonsmooth, multidimensional data. In *2017 ieee global conference on signal and information processing (globalsip)*

(p. 244-248). doi: 10.1109/GlobalSIP.2017.8308641

Craven, M., Allison, I., Fricker, H. A., & Warner, R. (2009). Properties of a marine ice layer under the amery ice shelf, east antarctica. *Journal of Glaciology*, *55*(192), 717–728. doi: 10.3189/002214309789470941

Fowler, A., & Ng, F. (2020). *Glaciers and ice sheets in the climate system: The karthaus summer school lecture notes*. Springer Nature.

Hulbe, C. L., Rignot, E., & Macayeal, D. R. (1998). Comparison of ice-shelf creep flow simulations with ice-front motion of filchner-ronne ice shelf, antarctica, detected by sar interferometry. *Annals of Glaciology*, *27*, 182–186. doi: 10.3189/1998AoG27-1-182-186

Jeong, S., Howat, I. M., & Bassis, J. N. (2016). Accelerated ice shelf rifting and retreat at pine island glacier, west antarctica. *Geophysical Research Letters*, *43*(22), 11,720-11,725. Retrieved from `https://agupubs.onlinelibrary.wiley.com/doi/abs/10.1002/2016GL071360` doi: https://doi.org/10.1002/2016GL071360

Jezek, K. C. (1984). A modified theory of bottom crevasses used as a means for measuring the buttressing effect of ice shelves on inland ice sheets. *Journal of Geophysical Research: Solid Earth*, *89*(B3), 1925-1931. Retrieved from `https://agupubs.onlinelibrary.wiley.com/doi/abs/10.1029/JB089iB03p01925` doi: https://doi.org/10.1029/JB089iB03p01925

LeB. Hooke, R. (1981). Flow law for polycrystalline ice in glaciers: Comparison of theoretical predictions, laboratory data, and field measurements. *Reviews of Geophysics*, *19*(4), 664-672. Retrieved from `https://agupubs.onlinelibrary.wiley.com/doi/`

abs/10.1029/RG019i004p00664 doi: https://doi.org/10.1029/RG019i004p00664

MacAyeal, D. R. (1989). Large-scale ice flow over a viscous basal sediment: Theory and application to ice stream b, antarctica. *Journal of Geophysical Research: Solid Earth*, *94*(B4), 4071-4087. Retrieved from https://agupubs.onlinelibrary.wiley.com/doi/abs/10.1029/JB094iB04p04071 doi: https://doi.org/10.1029/JB094iB04p04071

MacAyeal, D. R., Rignot, E., & Hulbe, C. L. (1998). Ice-shelf dynamics near the front of the filchner-ronne ice shelf, antaretica, revealed by sar interferometry: model/interferogram comparison. *Journal of Glaciology*, *44*(147), 419–428. doi: 10.3189/S0022143000002744

Morlighem, M. (2020). *Measures bedmachine antarctica, version 2.* NASA National Snow and Ice Data Center Distributed Active Archive Center. Retrieved from https://nsidc.org/data/NSIDC-0756/versions/2 doi: 10.5067/E1QL9HFQ7A8M

Morlighem, M., Rignot, E., Binder, T., Blankenship, D., Drews, R., Eagles, G., . . . others (2020). Deep glacial troughs and stabilizing ridges unveiled beneath the margins of the antarctic ice sheet. *Nature Geoscience*, *13*(2), 132–137.

Mouginot, J., Rignot, E., Scheuchl, B., & Millan, R. (2017). Comprehensive annual ice sheet velocity mapping using landsat-8, sentinel-1, and radarsat-2 data. *Remote Sensing*, *9*(4). Retrieved from https://www.mdpi.com/2072-4292/9/4/364 doi: 10.3390/rs9040364

Mouginot, J., Scheuchl, B., & Rignot, E. (2012). Mapping of ice motion in antarctica using synthetic-aperture radar data. *Remote Sensing*, *4*(9), 2753–2767. Retrieved from https://www.mdpi.com/2072-4292/4/9/2753 doi: 10.3390/rs4092753

Nicholls, K. W., Corr, H. F., Stewart, C. L., Lok, L. B., Brennan, P. V., & Vaughan, D. G. (2015). A ground-based radar for measuring vertical strain rates and time-varying basal melt rates in ice sheets and shelves. *Journal of Glaciology*, *61*(230), 1079–1087. doi: 10.3189/2015JoG15J073

Nye, J. F. (1955). Comments on dr. loewe's letter and notes on crevasses. *Journal of Glaciology*, *2*(17), 512–514. doi: 10.3189/S0022143000032652

Reeh, N. (1968). On the calving of ice from floating glaciers and ice shelves. *Journal of Glaciology*, *7*(50), 215–232. doi: 10.3189/S0022143000031014

Rignot, E., & MacAyeal, D. R. (1998). Ice-shelf dynamics near the front of the filchner—ronne ice shelf, antarctica, revealed by sar interferometry. *Journal of Glaciology*, *44*(147), 405–418. doi: 10.3189/S0022143000002732

Rignot, E., Mouginot, J., & Scheuchl, B. (2011). Ice flow of the antarctic ice sheet. *Science*, *333*(6048), 1427-1430. Retrieved from https://www.science.org/doi/abs/10.1126/science.1208336 doi: 10.1126/science.1208336

Rignot, E., Mouginot, J., & Scheuchl, B. (2017). *Measures insar-based antarctica ice velocity map, version 2.* NASA National Snow and Ice Data Center Distributed Active Archive Center. Retrieved from https://nsidc.org/data/NSIDC-0484/versions/2 doi: 10.5067/D7GK8F5J8M8R

Rist, M. A., Sammonds, P. R., Oerter, H., & Doake, C. S. M. (2002). Fracture of antarctic shelf ice. *Journal of Geophysical Research: Solid Earth*, *107*(B1), ECV 2-1-ECV 2-13. Retrieved from https://agupubs.onlinelibrary.wiley.com/doi/

abs/10.1029/2000JB000058 doi: https://doi.org/10.1029/2000JB000058

Robin, G. d. Q. (1955). Ice movement and temperature distribution in glaciers and ice sheets. *Journal of Glaciology*, *2*(18), 523–532. doi: 10.3189/002214355793702028

Sandhäger, H., Rack, W., & Jansen, D. (2005). Model investigations of larsen b ice shelf dynamics prior to the breakup. *FRISP Rep*, *16*, 5–12.

Sergienko, O. V. (2014). A vertically integrated treatment of ice stream and ice shelf thermodynamics. *Journal of Geophysical Research: Earth Surface*, *119*(4), 745-757. Retrieved from https://agupubs.onlinelibrary.wiley.com/doi/abs/10.1002/2013JF002908 doi: https://doi.org/10.1002/2013JF002908

Sergienko, O. V., Goldberg, D. N., & Little, C. M. (2013). Alternative ice shelf equilibria determined by ocean environment. *Journal of Geophysical Research: Earth Surface*, *118*(2), 970-981. Retrieved from https://agupubs.onlinelibrary.wiley.com/doi/abs/10.1002/jgrf.20054 doi: https://doi.org/10.1002/jgrf.20054

Taylor, J. R. (1982). *An introduction to error analysis: the study of uncertainties in physical measurements* (Vol. 2). Springer.

Thomas, R. H., & MacAyeal, D. R. (1982). Derived characteristics of the ross ice shelf, antarctica. *Journal of Glaciology*, *28*(100), 397–412. doi: 10.3189/S0022143000005025

Tyler, S., Holland, D., Zagorodnov, V., Stern, A., Sladek, C., Kobs, S., ... Bryenton, J. (2013). Using distributed temperature sensors to monitor an antarctic ice shelf and sub-ice-shelf cavity. *Journal of Glaciology*, *59*(215), 583–591. doi: 10.3189/2013JoG12J207 van den Broeke, M. (2008). Depth and density of the antarctic firn layer. *Arctic, Antarctic, and Alpine Research*, *40*(2), 432–438.

van Wessem, J. M., van de Berg, W. J., Noël, B. P. Y., van Meijgaard, E., Amory, C., Birnbaum, G., ... van den Broeke, M. R. (2018). Modelling the climate and surface mass balance of polar ice sheets using racmo2 – part 2: Antarctica (1979–2016). *The Cryosphere*, *12*(4), 1479–1498. Retrieved from https://tc.copernicus.org/articles/12/1479/2018/ doi: 10.5194/tc-12-1479-2018

Wagner, T. J. W., James, T. D., Murray, T., & Vella, D. (2016). On the role of buoyant flexure in glacier calving. *Geophysical Research Letters*, *43*(1), 232-240A. Retrieved from https://agupubs.onlinelibrary.wiley.com/doi/abs/10.1002/2015GL067247 doi: https://doi.org/10.1002/2015GL067247

Walker, C. C., Bassis, J. N., Fricker, H. A., & Czerwinski, R. J. (2013). Structural and environmental controls on antarctic ice shelf rift propagation inferred from satellite monitoring. *Journal of Geophysical Research: Earth Surface*, *118*(4), 2354-2364. Retrieved from https://agupubs.onlinelibrary.wiley.com/doi/abs/10.1002/2013JF002742 doi: https://doi.org/10.1002/2013JF002742

Wearing, M. G. (2017). The flow dynamics and buttressing of ice shelves phd thesis.

Weertman, J. (1957). Deformation of floating ice shelves. *Journal of Glaciology*, *3*(21), 38–42. doi: 10.3189/S0022143000024710

Wuite, J., Hetzenecker, M., Nagler, T., & Scheiblauer, S. (2021). *Esa antarctic ice sheet climate change initiative (antarctic_ice_sheet_cci): Antarctic ice sheet monthly velocity from 2017 to 2020, derived from sentinel-1,* *v1.* NERC EDS Centre for Environmental Data Analysis. Retrieved from https://dx.doi.org/10.5285/00fe090efc58446e8980992a617f632f doi: 10.5285/00fe090efc58446e8980992a617f632f

Zarrinderakht, M., Schoof, C., & Peirce, A. (2022). The effect of hydrology and crevasse wall contact on calving. *The Cryosphere*, *16*(10), 4491–4512. Retrieved from https://tc.copernicus.org/articles/16/4491/2022/ doi: 10.5194/tc-16-4491-2022

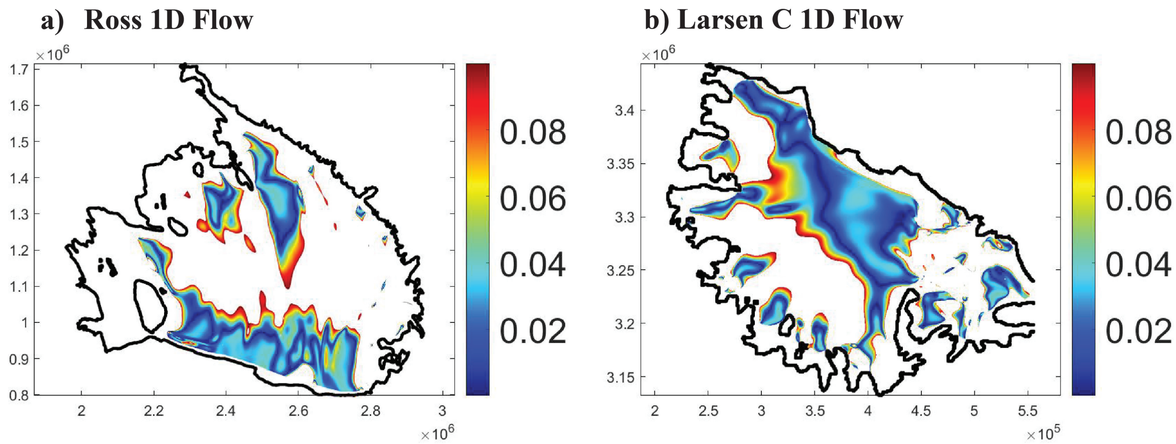

Figure S1. Regions where the background viscous ice flow is approximately 1D based on equation (S2). Rifts in these regions are regarded as having formed due to 1D tension, called Mode I failure. The color scale is dimensionless strain rate deviation from 1D flow as in equation (S2), and the axes are in units of meters.

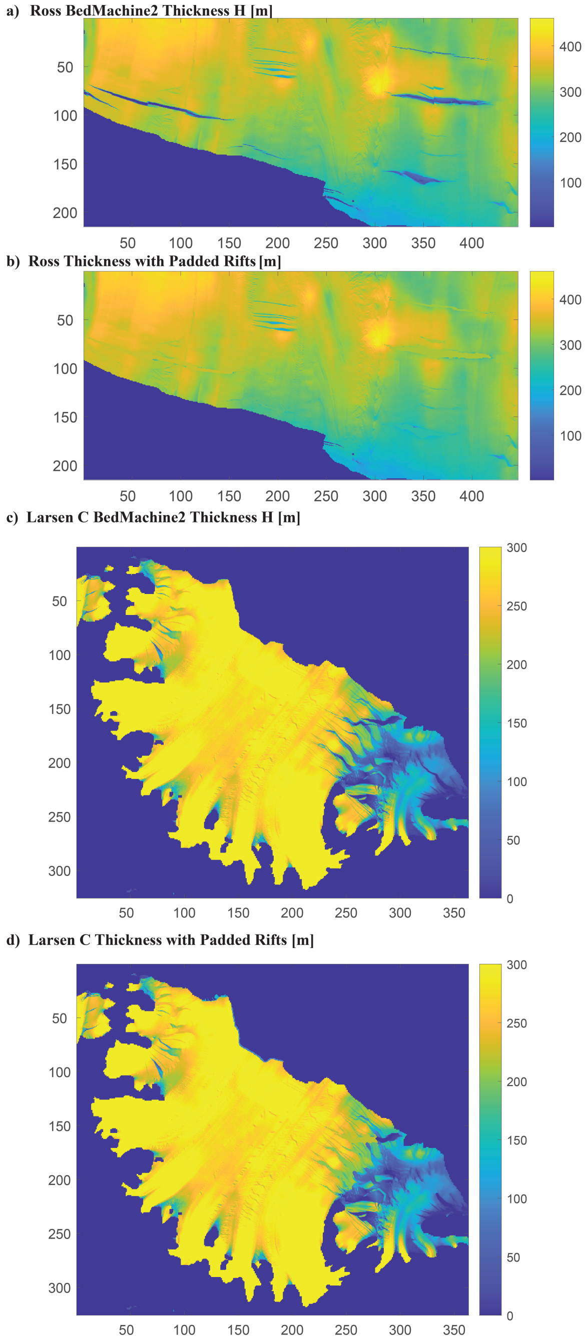

Figure S2. Mélange padding in kilometers with local, unbroken ice thickness on the RIS and LCIS. Subfigures a) and c) are the original data products from BedMachine2, while subfigures b) and d) are the mélange-padded results used in this study to see if fracture theories can correctly predict rifts in areas where they are known to have occurred. LCIS thickness has an upper bound of 300 meters in the color bars of subfigures c) and d) to enhance the visibility of padded rifts.

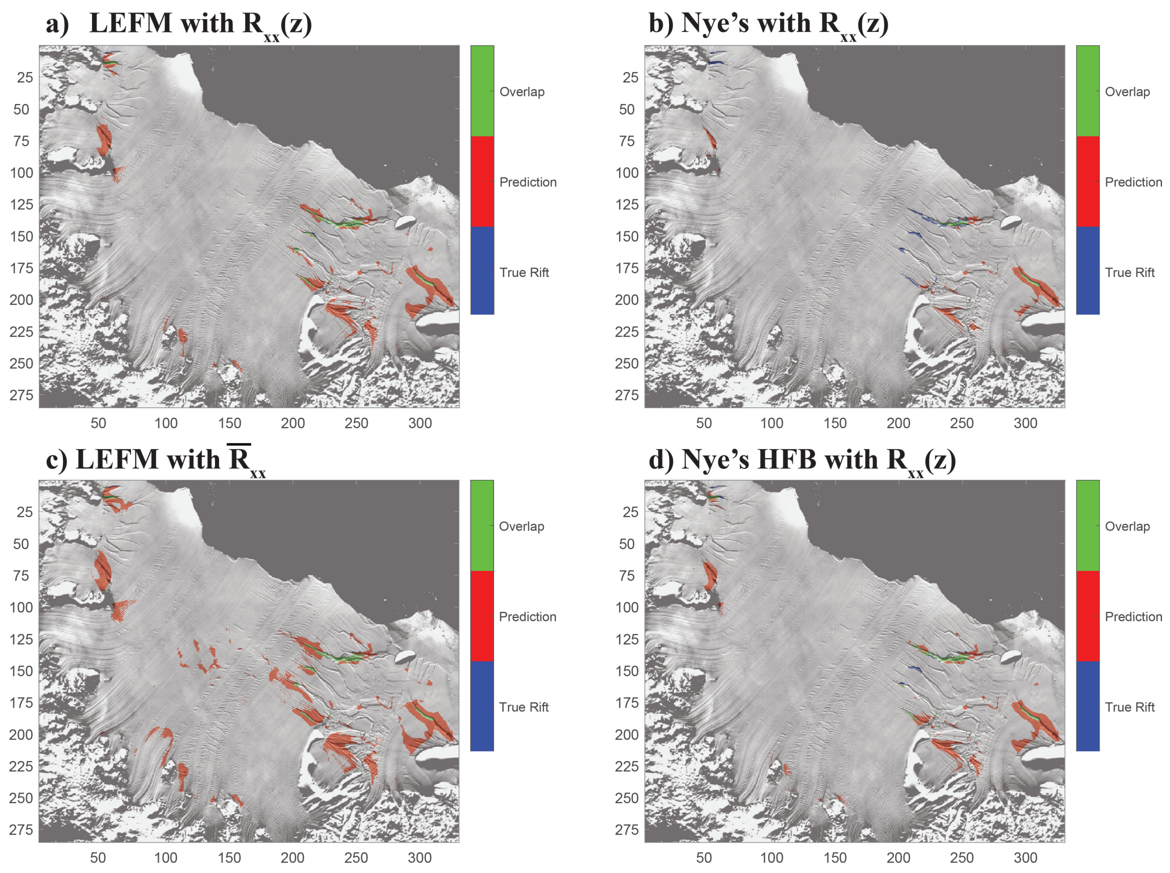

Figure S3. Same as Figure 3, except on LCIS.

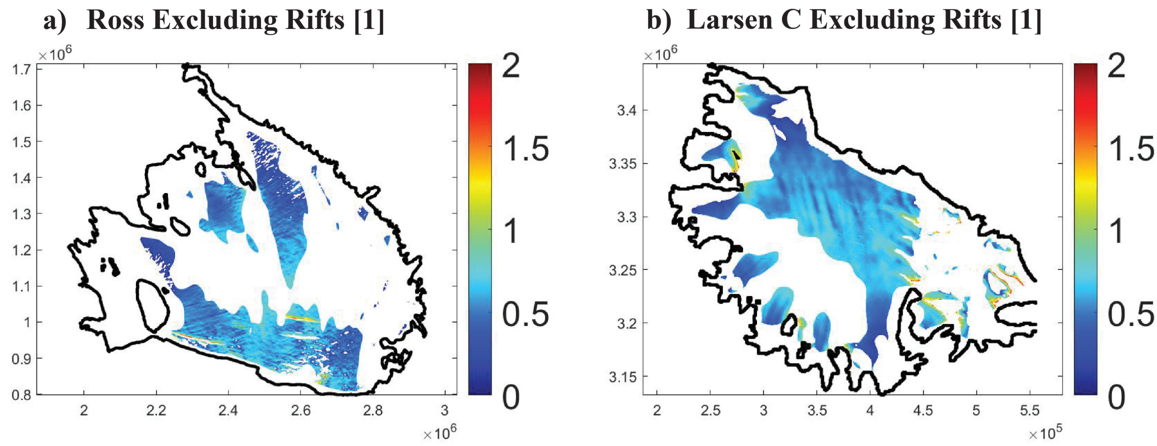

Figure S4. Extensional, approximately 1D regions of RIS and LCIS that exclude both observed rifts and rifts predicted by a resistive stress greater than twice the freely-floating resistive stress. The color shows the magnitude of $\overline{R}_{xx}/\overline{R}_{xx}^{IT}$.

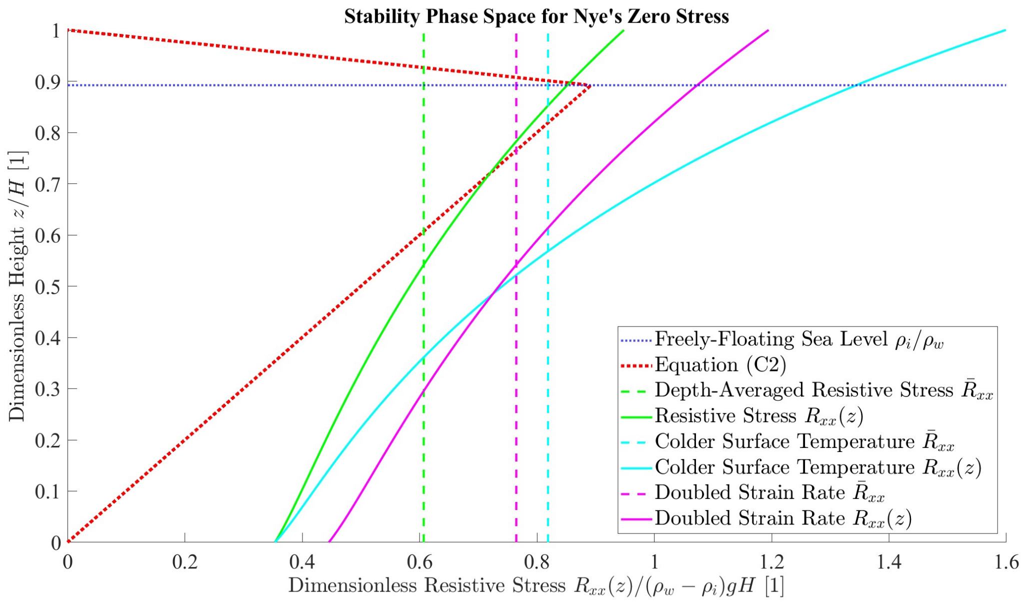

Figure S5. Visualizing Nye's Zero-Yield Stress condition. The dotted red curve, defined by the piecewise distribution in equation (S4), is the magnitude of the lithostatic pressure minus water pressure that opposes fracture; the intersection below sea level of a given resistive stress with the dotted red curve determines basal crevasse depth. Solid curves utilize $R_{xx}(z)$, whereas dashed lines utilize $\overline{R}_{xx}$. Green curves with surface temperature T_s=-22°C are the reference for cyan and magenta curves; cyan curves utilize T_s=-32°C, and magenta curves have along-flow strain rate doubled. Depth-averaged resistive stresses have unstable basal crevassing occur only at sea level, and may be solved for analytically; vertical temperature profiles may have crevasses unstably propagate before sea level, and require numerical treatment.

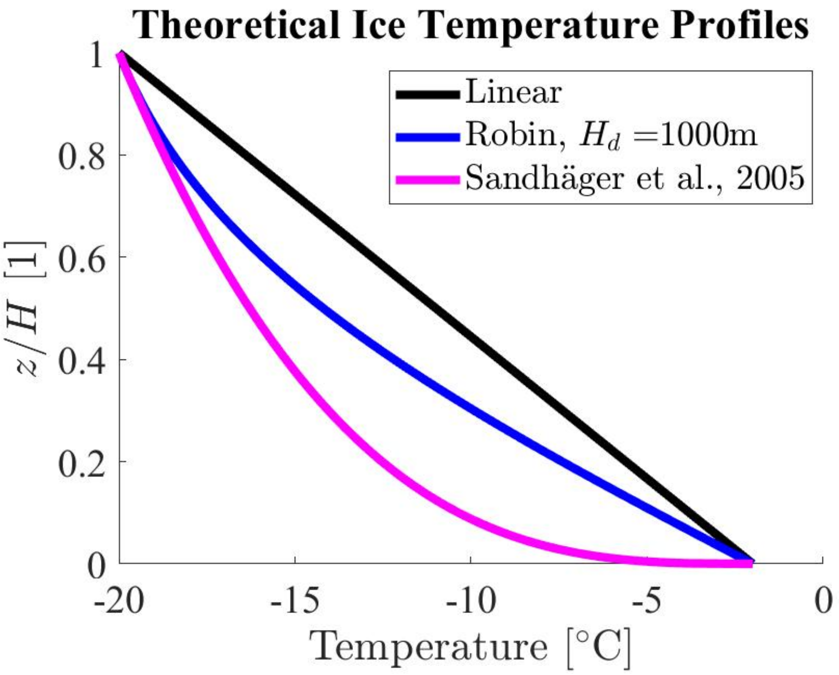

Figure S6. Theoretical ice shelf temperature profiles. The body of the paper uses a linear temperature profile, while this Appendix section treats a Robin profile.

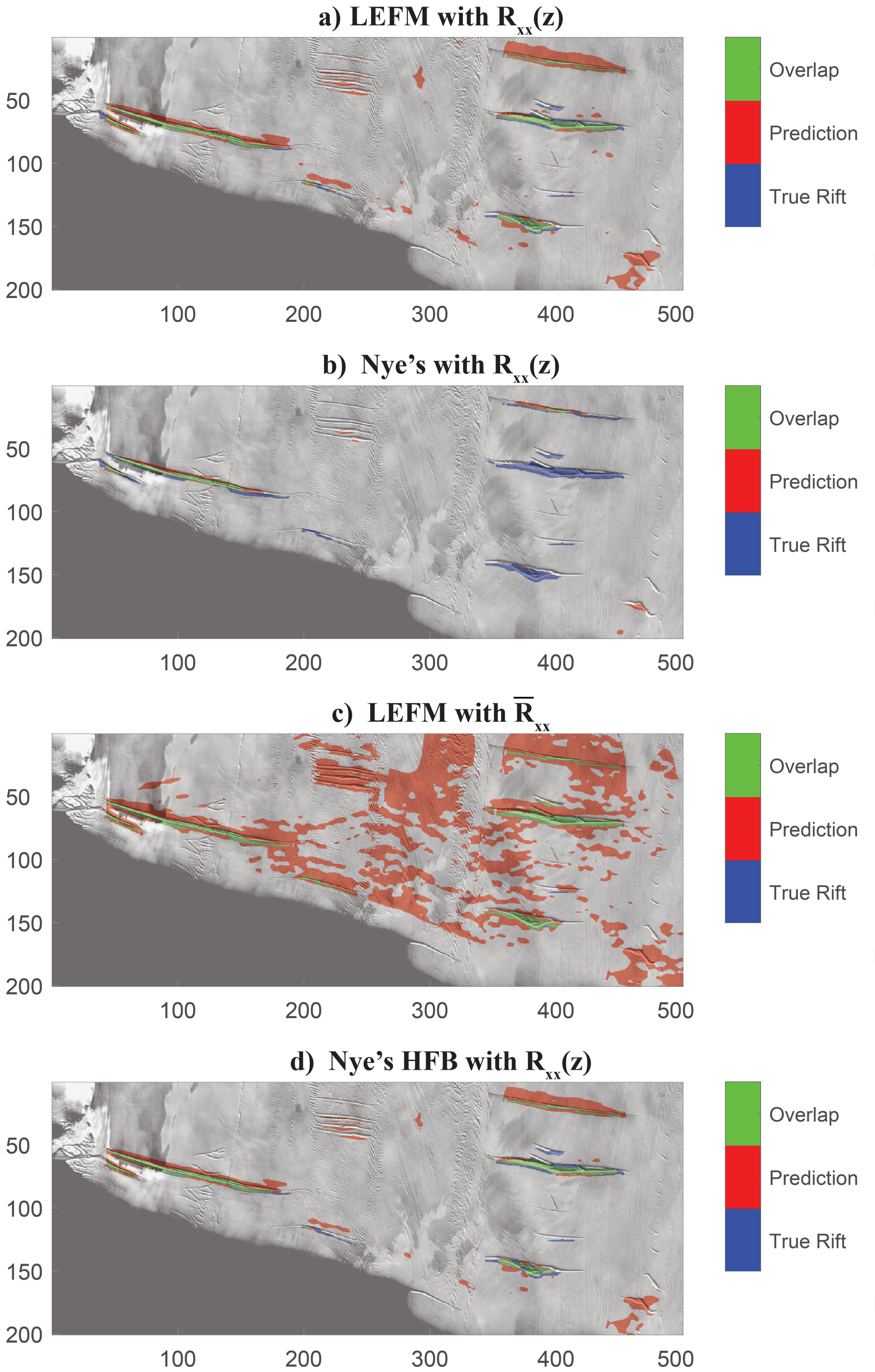

Figure S7. The same map view plot in kilometers as Figure 3, except that a Robin temperature profile is taken to generate the rift formation stresses and assumed in calculating the value of stress in the data.

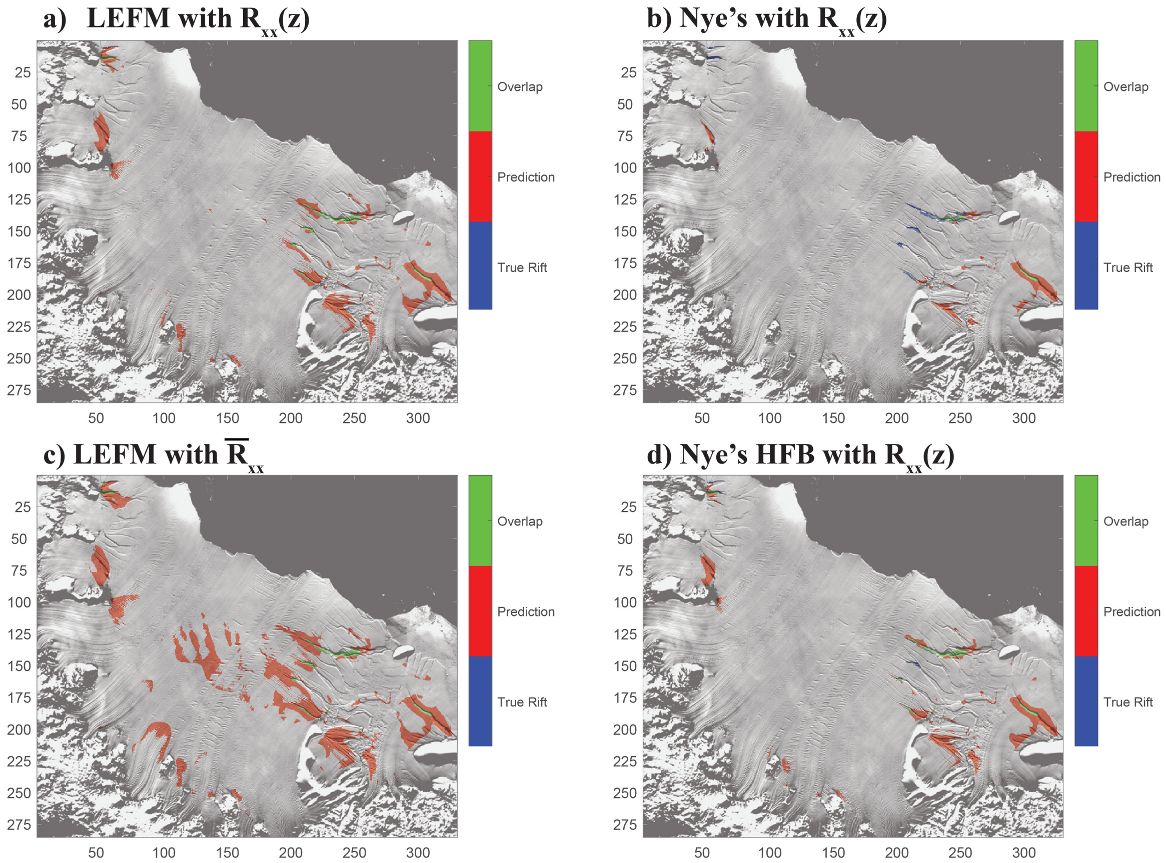

Figure S8. Following Figure S7, we use the same concept as Figure S3, except that a Robin temperature profile is used to generate the rift formation stresses and assumed in calculating the stress values of the data.

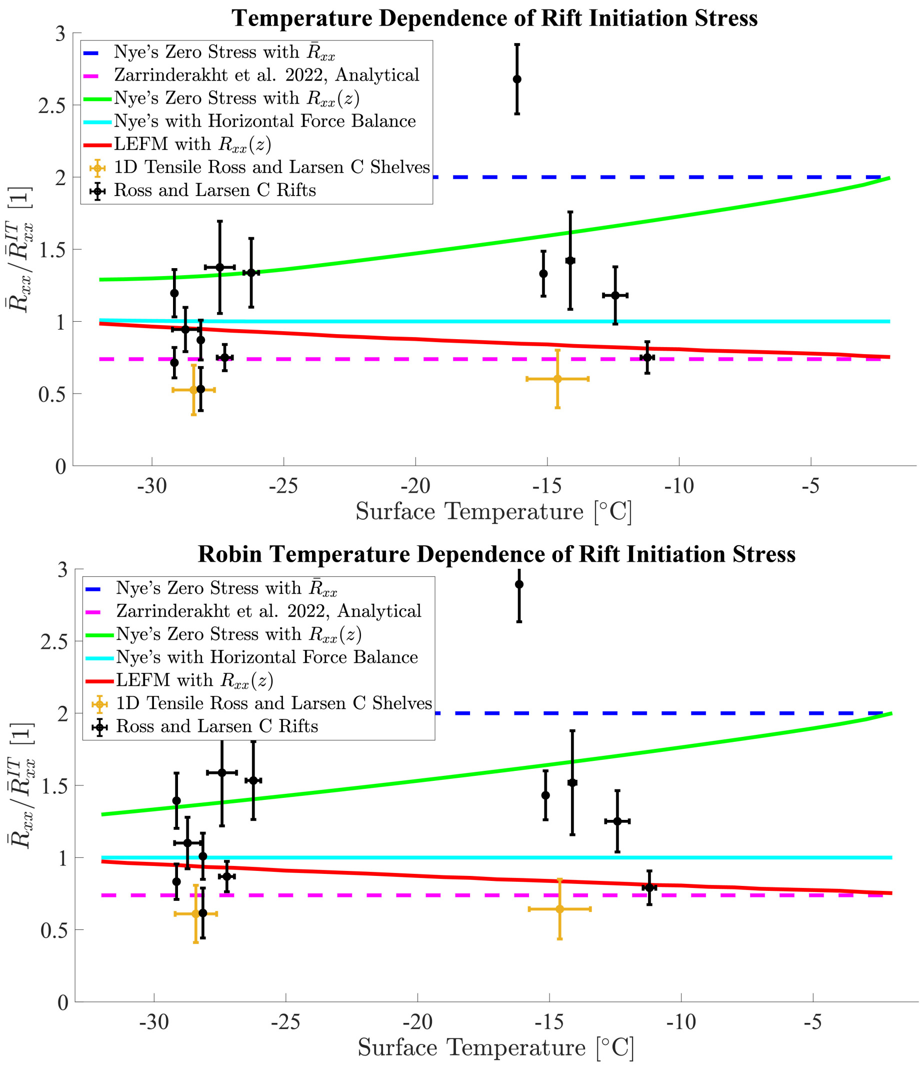

Figure S9. The same idea as Figure 4, except that we include approximate rift stress data and evaluate linear and Robin temperature profiles for generating the depth-dependent rift formation stresses (green, cyan, and red curves). Relative to the linear temperature profile, the Robin profile raises the value of the resistive stresses in the rifts and non-rift ice shelf data sets (black and orange data, respectively), but has a negligible effect on the rifting stress threshold curves. Nye's with Horizontal Force Balance is a much more accurate rift initiation theory compared with Nye's original theory, and is largely or fully insensitive to surface temperature assuming a linear or Robin profile. This provides robustness, as the same conclusions are drawn with either a linear or Robin temperature profile.

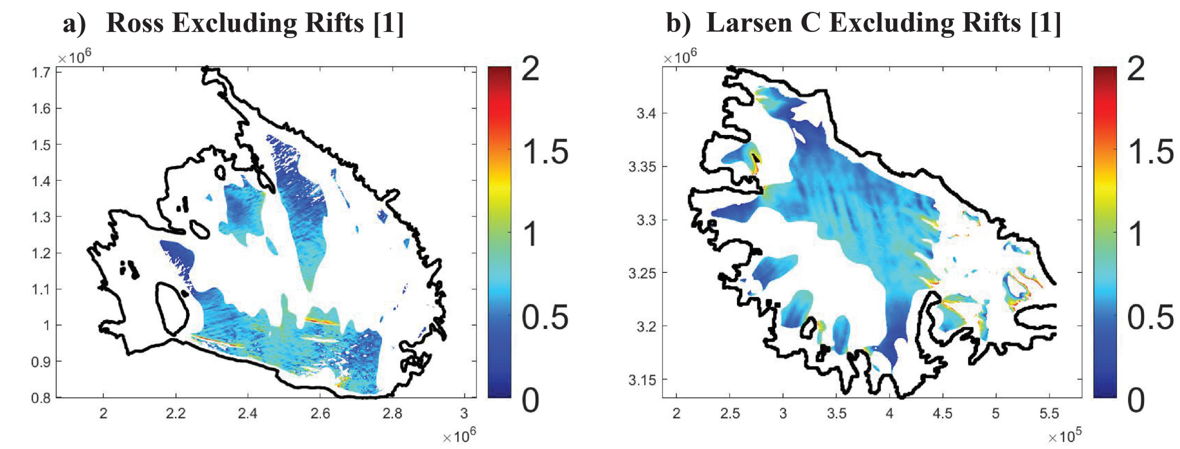

Figure S10. The same as Figure S4, except that the Robin temperature profile raises the value of the depth-averaged resistive stress relative to the linear temperature profile.

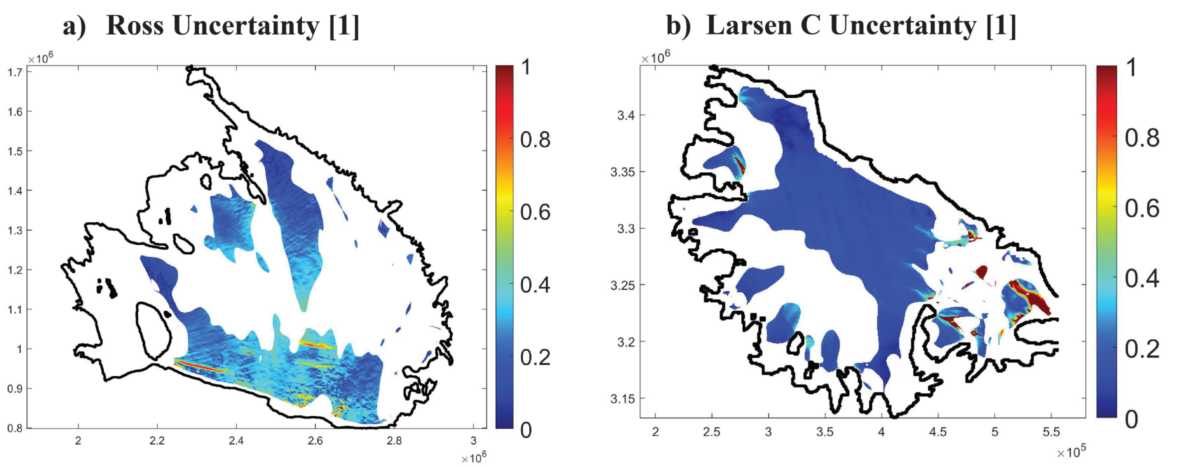

Figure S11. Estimates of dimensionless resistive stress uncertainty σ_β defined in equation (S22) on RIS and LCIS, with thickness padded for known rifts. The small uncertainty on LCIS provides more confidence in our work. The color scale is capped at $\sigma_\beta = 1$, while there are a few outliers due to thickness uncertainty being comparable or larger than ice thickness.